Nano Energy 44 (2018) 144–154

Contents lists available at ScienceDirect

Nano Energy

journal homepage: www.elsevier.com/locate/nanoen

Communication

N-doped graphdiyne for high-performance electrochemical electrodes

Hong Shang[a], Zicheng Zuo[a,*], Haiyan Zheng[b], Kuo Li[b], Zeyi Tu[a], Yuanping Yi[a], Huibiao Liu[a], Yongjun Li[a], Yuliang Li[a,*]

[a] Beijing National Laboratory for Molecular Sciences (BNLMS), CAS Research/Education Center for Excellence in Molecular Sciences, CAS Key Laboratory of Organic Solids, Institute of Chemistry, Chinese Academy of Sciences, Beijing 100190, PR China
[b] Center for High Pressure Science and Technology Advanced Research, Beijing 100094, PR China

ARTICLE INFO

Keywords:
Graphdiyne
Porous carbon
Supercapacitor
Oxygen reduction reaction
2D material

ABSTRACT

A novel method is developed for constructing well-defined N-doped graphdiyne (GDY) nanostructures. This method can effectively tune the N-configurations (pyridinic N and triazine-like N cluster), N-content, and porous structures of GDYs, indicating good controllability. The N-configurations and structure of GDYs are well confirmed by the X-ray photoelectron spectrometer measurements, nitrogen absorption measurements and neutron pair distribution function (PDF), respectively. The as-prepared GDYs can be assembled into high-performance two-electrode supercapacitors with specific capacitance high up to 250 F g^{-1}, delivering an energy density of 8.66 Wh kg^{-1} and power density of 19.3 kW kg^{-1}; the well-defined N-configuration in GDYs offers us an opportunity to understand the controversial nitrogen role in catalyzing the oxygen reduction reaction in sp^2 carbons. Importantly, this method for creating well-defined N-doped GDYs may widely extend the GDY materials for new energy fields.

1. Introduction

Graphdiyne (GDY), 2-dimensional (2D) all-carbon material from the sp^2 and sp-carbon, has attracted broad interests and achieved substantial progresses, since it was first prepared in 2010 [1,2]. Compared to the prevailing sp^2 carbon materials (graphene, carbon nanotube) by high-temperature, low-efficient, and high-cost methods, the preparation of graphdiyne in a moderate condition in liquid phase has obvious superiorities, which is possible to solve the scientific problems in lithium-ion batteries, supercapacitors, photovoltaic devices, as well as catalysts [3–5]. For example, nanofilm, nanotube and nanoparticles of graphdiyne can be formed by self-assembly for realizing some special applications [1,6–8]. Due to the advantages of bottom-up strategy for constructing GDY under low temperature, the acetylene-rich GDY may become one of the first stable 2D artificial all-carbon materials possessing a tunable bandgap and high electronic density, thus enhancing the interaction with the active metal and metal oxides and facilitating electronic migration in the reactions [9,10]. Such properties can hardly be obtained from the bare graphene and carbon nanotube. Besides, the linear rigidity of the diyne linkage offers graphdiyne in-plane pores with particular selectivity, which may be another great advantage for the all carbon material with the sp^2 and sp hybridized carbon atoms in electrochemical energy storages.

As an artificial carbon material with good theoretical properties, the state-of-the-art heteroatom-doping approaches are implemented in tuning its characters for further performances in electrochemical devices [11–13], similar with those in the prevalent all-carbon materials [14–18]. Via the reported methods carried out in extreme conditions, it realizes the performance enhancement, but hasn't yet fully displayed the stronger editability of 2D graphdiyne for some imperative applications. Such extreme approaches leave the challenges in controlling heteroatom content and doping configurations like that in prevailing sp^2 carbons [15,19–21], and it is difficult to break through the controversy in recognizing the active role of heteroatoms.

Herein, the good editability of GDY is shown by a novel method for tailoring its N-doping configuration, N-content, and micropores. Via our solvent- and metal-catalyst-free method in air at 120 °C, single N and triazine-like N cluster are successfully introduced into GDYs. The as-prepared GDYs possess high surface area and good 3D continuousness, and are utilized as high-performance supercapacitor electrodes, delivering a high energy density (8.66 Wh kg^{-1}) and power density (19.3 kW kg^{-1}) in a two-electrode device. Meanwhile, it shows a good performance in catalyzing oxygen reduction reaction (ORR). The well-defined N-configuration in GDYs provides us an opportunity to understand the N roles in catalyst, and gives some inspirations to answer the controversial mechanisms in the traditional N-doped sp^2 carbons [19,21]. Moreover, the structural editable GDY might help us to create more on-demand carbon materials and nanocomposites for solving

* Corresponding authors.
E-mail addresses: zuozic@iccas.ac.cn (Z. Zuo), ylli@iccas.ac.cn (Y. Li).

https://doi.org/10.1016/j.nanoen.2017.11.072
Received 11 August 2017; Received in revised form 2 November 2017; Accepted 30 November 2017
Available online 06 December 2017

some difficult problems in the ever-growing new energy fields.

2. Experimental methods

2.1. General remarks

Tetrabutylammonium fluoride (TBAF) was purchased from Alfa Aesar. Potassium fluoride, hexabromobenzene, perchloropyridine and cyanuric chloride were obtained from J&K Scientific. Toluene and tetrahydrofuran (THF) were redistilled under argon reflux with Na crumbs. Unless otherwise specified, all other reagents were purchased commercially from Sinopharm Chemical Reagent and used without further purification. All aqueous solutions were prepared with Milli-Q water. Cyanuric[(trimethylsilyl)ethynyl] (CTMSE), Hexakis[(trimethylsilyl)ethynyl]benzene (HTMSEB), and Pentakis[(trimethylsilyl) ethynyl]pyridine (PTMSEP) and were synthesized according to our previous report [1].

2.2. Preparation of N0-GDY, N1-GDY, and N3-GDY

To a solution of the precursor (HTMSEB, PTMSEP, CTMSE) (0.1 mmol) in THF (30 ml) was added TBAF (0.8 ml, 1 M in THF, 0.8 mmol) and stirred at 0 °C for 10 min, respectively. The solution was then diluted with ethyl ether and washed with brine and dried with anhydrous Na_2SO_4. The solvent was removed in vacuo and grey white powder was obtained. Then the powder was transferred slowly into a 120 °C preheated conical flask in the air, and an ultrafast reaction with a slight explosion in seconds was took place and deep black GDYs was obtained without further treatment for following characterizations. For N3-GDY, the reaction intensity is obviously reduced owing to decrease of the amount of ethynyl in unit molecular, despite the phenomenon of slight combustion.

2.3. DFT calculation

The monolayer models were built with 20 Å vacuum layer thickness along nonperiodical directions. Geometry optimization (both atomic coordinates and cell parameters) and band structure calculations were carried out using VASP package. The PBE exchange-correlation functional within a generalized gradient approximation and the projector augmented-wave potential were employed. The plane wave energy cutoff was set to 600 eV. Uniform $15\times15\times1$, $14\times8\times1$ and $9\times9\times1$ Gamma centered Monkhorst-Pack k-point meshes were employed for N0-GDY, N1-GDY and N3-GDY.

2.4. Characterization

Scanning electron microscopy (SEM) images were recorded using a Hitachi Model S-4800 field emission scanning electron microscope. TEM and HRTEM were performed on a JEM-2100F electron microscope with an accelerating voltage of 200 kV. XPS was performed on a Thermo Scientific ESCALab 250Xi instrument and 200 W monochromated Al Kα radiation. The binding energies obtained in the XPS analyses were corrected with reference to C1s (284.8 eV). XRD data were collected using a Japan Rigaku D/max-2500 rotation anode X-ray diffractometer and graphite-monochromated Cu Kα radiation (λ = 1.54178 Å). Raman spectra were recorded at a resolution of 2 cm^{-1} using a Renishaw-2000 Raman spectrometer, with the 514.5 nm line of an Ar ion laser as the excitation source. All the samples were no further treatment prior to measurements.

2.5. Neutron pair distribution function (PDF)

The neutron PDF data was obtained at Nanoscale-Ordered Materials Diffractometer (NOMAD), Spallation Neutron Source (SNS), Oak Ridge National Laboratory (ORNL) [22]. A combination of the wide wavelength band and the high detector coverage of NOMAD allowed us to obtain high quality PDFs at Qmax as high as 31.4 $Å^{-1}$. The samples were measured in 3 mm quartz capillaries at room temperature. The measurements were performed in an argon atmosphere to reduce scattering from the air. In order to obtain the structure factor S(Q), the background was subtracted and data was normalized by the scattering from the solid vanadium rod. Diamond measurements were used to calibrate detectors prior to all measurements. The IDL based NOMAD specific software has been used to reduce the data and obtain a PDF. The simulation of the PDF data was done using the PDFgui software package [23].

2.6. Electrochemical measurements

For evaluating the supercapacitor performance of GDYs, the 95% samples are uniformly mixed with the PVDF binder (5%) in the N-Methyl pyrrolidone solution, and the as-prepared solution is uniformly coating on the nickel foam with an average area-loading of 2 mg cm^{-2}. The supercapacitors based on the GDYs are assembled in a symmetrical two-electrode configuration in the coin cell using the 7.0 M KOH aqueous electrolyte. The filter paper is used as separator. The electrochemical impedance spectra (EIS), cyclic voltammograms (CV) and galvanostatic charge/discharge curves were all taken using a CHI 660D electrochemical station, and the EIS is tested in the frequency range of 100 kHz–0.1 Hz with a 5 mV ac amplitude, cyclic voltammetry and galvanostatic charge/discharge measurements of all the cells were performed over the potential range of 0–1.0 V.

Gravimetric capacitance for a single electrode was calculated from galvanostatic charge/discharge curves

$$C_s = \frac{4I\Delta t}{m\Delta V}$$

where I is the constant current and m is the total mass for electrodes, Δt is the discharge time and ΔV is the voltage change during the discharge process.

The energy density was calculated by following equation

$$E = \frac{C_s V^2}{8}$$

The average power density is given by

$$P_{av} = \frac{E}{\Delta t}$$

Δt is the discharge time.

For testing oxygen reduction reaction, 93% of the as-prepared GDYs (2 mg) are uniformly blended with 7% Nafion in the isopropanol solution (1 ml) before the experiments. After then, the samples (20 μL) are drop-coating on the rotating disk electrode (d = 5 mm), and dried naturally. The experiments are carried out in the 0.1 M KOH aqueous solution. The CV and linear sweep voltammetry (LSV) are both performed on a CHI 660D electrochemical station.

The Koutechy-Levich plot derived from LSV curves shows following relationship at different working potential:

$$\frac{1}{j} = \frac{1}{j_k} + \frac{1}{B\omega^{0.5}}$$

in which j is the current density at the applied voltage, j_k is the kinetic current, and ω is the angular velocity, B is the parameter, has the following relationship with electron transfer number

$$B = 0.62nF\left(D_{O_2}\right)^{2/3}\nu^{-1/6}C_{O_2}$$

in which n represents the overall electron transfer number per oxygen molecule, F is the Faraday constant with the value of 96485 C mol^{-1}, D_{O2} is the diffusion coefficient of O_2 in 0.1 M KOH aqueous solution; ν is the kinetic viscosity (0.01 $cm^2\,s^{-1}$); and C_{O2} is the bulk concentration of O_2 (1.2×10^{-6} mol cm^{-3}).

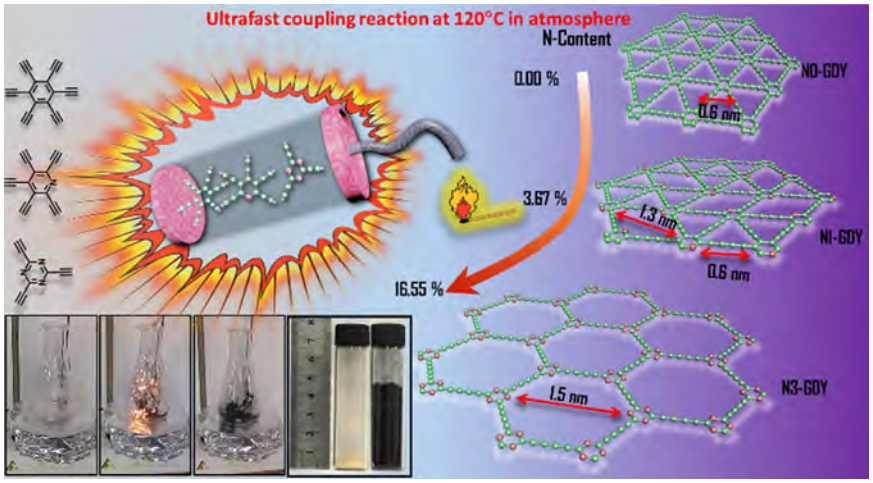

Scheme 1. a) Schematic illustration of preparation processes and b) representation structures of the N0-GDY, N1-GDY and N3-GDY.

3. Result and discussion

The coupling reaction between end acetylenic groups have been well performed in solvent system with and without oxygen [24], chemical vapor deposition method [25], and solid phase reaction by ball mill [26]. Inspired by these methods, the solid phase reactions were carried out in air under a suitable temperature without any additives, accompanied by intensive explosion phenomenon (Supporting Video). Such phenomenon probably indicates that the present of oxygen can accelerate removal of hydrogen and the cross-coupling reaction at 120 °C. Scheme 1 depicts the advantages of the method for ultrafast preparation of the well-defined N-doped GDY. The precursor of HTMSEB, PTMSEP, CTMSE with 0, 1, and 3 nitrogen atoms were predesigned and synthesized, respectively, and the corresponding samples were named of N0-GDY, N1-GDY, and N3-GDY (shown in Scheme 1). The sample from the mixture of PTMSEP and CTMSE is named of N2-GDY.

Supplementary material related to this article can be found online at: http://dx.doi.org/10.1016/j.nanoen.2017.11.072.

Ideally, the size of the in-plane openings can be well controlled, with the addition of N atom instead of the acetylenic branches. The in-plane selectivity might be tuned via this way. For further showcasing the editability, the sample N2-GDY is synthesized by using the precursor mixtures of PTMSEP and CTMSE with equal stoichiometric ratio (Fig. S1 and S2, Supporting information). The inset photo in Scheme 1 representatively demonstrates the significant color and volume changes after the ultrafast cross-coupling reaction.

The structural variation in GDYs will influence the electronic properties, and the density functional theory (DFT) is applied to calculate the band structure of the three samples. In Fig. 1, the DFT-calculated band structure show that all the three monolayer materials are direct band gap (all at Γ point) semiconductors, and the N addition increases the band gap of GDY. The band-gap energy of N3-GDY (2.30 eV) is much larger than those of N0-GDY (0.48 eV) and N1-GDY (0.49 eV) graphdiyne. Besides, significant differences in dispersion relationship are also observed. The valance and conduction bands of N0-GDY and N1-GDY are obviously more dispersive than those of N3-GDY. It is worth mentioning that the highest occupied and lowest unoccupied bands of N3-GDY are almost flat along the whole Brillouin Zone path. The diverse electronic properties of the three monolayer materials indicate that 2D GDY has adequate band gap to be edited for the on-demand requirements, and the N-doping strategy is an efficient approach to tune its band gap.

The as-prepared GDYs are examined using X-ray diffraction (XRD, Fig. 2a). Samples N0-GDY, N1-GDY and N3-GDY all show a broad peak around 23°, ascribing to the typical interlayer distance of 2D carbon materials. The regular shift from N0-GDY to N1-GDY, and to N3-GDY is probably caused by the gradually reduced π conjugation and π-π stacking, which means that the interlayer distance is swelled. Raman spectroscopy is a useful technique for characterizing the carbon-containing materials and also for evaluating the quality and uniformity of GDYs. All of the Raman spectra display two prominent peaks attributed

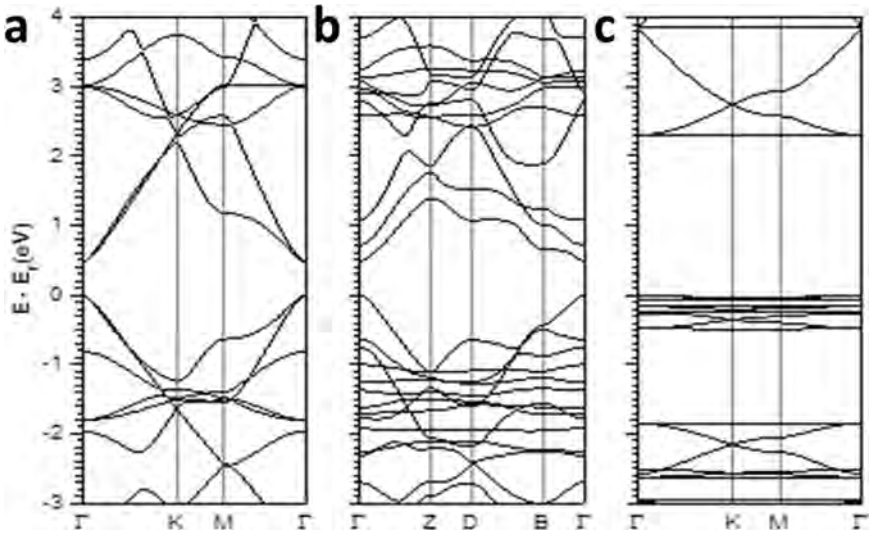

Fig. 1. Electronic band structure of a) N0-GDY, b) N1-GDY and c) N3-GDY. Points of high symmetry in the first Brillouin zone are labelled as follows: for N0-GDY and N3-GDY, Γ(0, 0, 0) , K(−1/3, 2/3, 0), M(0, 1/2, 0); for N1-GDY, Γ(0, 0, 0) , Z(1/2, 0, 0), D(1/2, −1/2, 0), B(0, −1/2, 0).

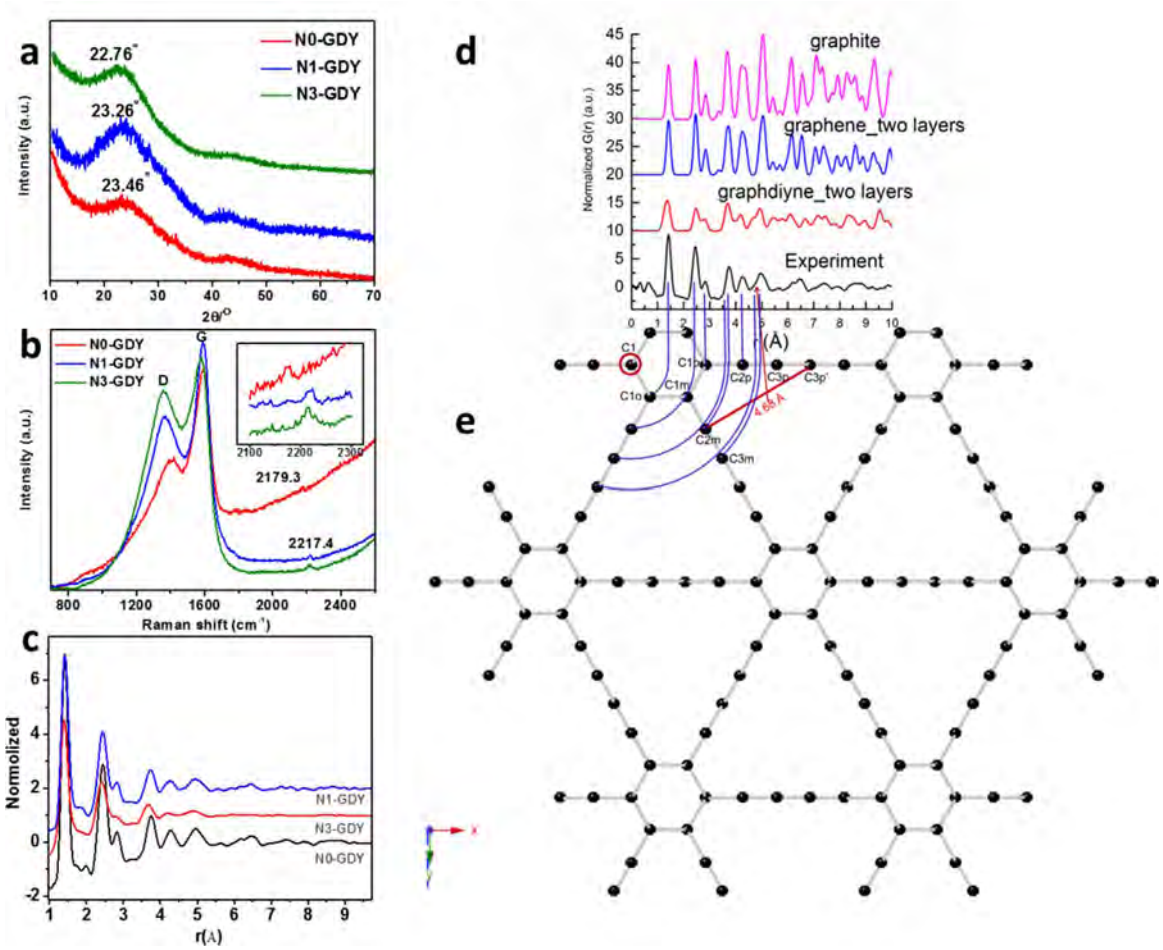

Fig. 2. a) XRD patterns, b) Raman spectra, and c) neutron pair distribution function (PDF) of N0-GDY, N1-GDY and N3-GDY; (d) Experimental and simulated neutron PDF of graphdiyne, graphene with two layers (calculated) and graphite (calculated) and (e) the peak assignment with the graphdiyne model.

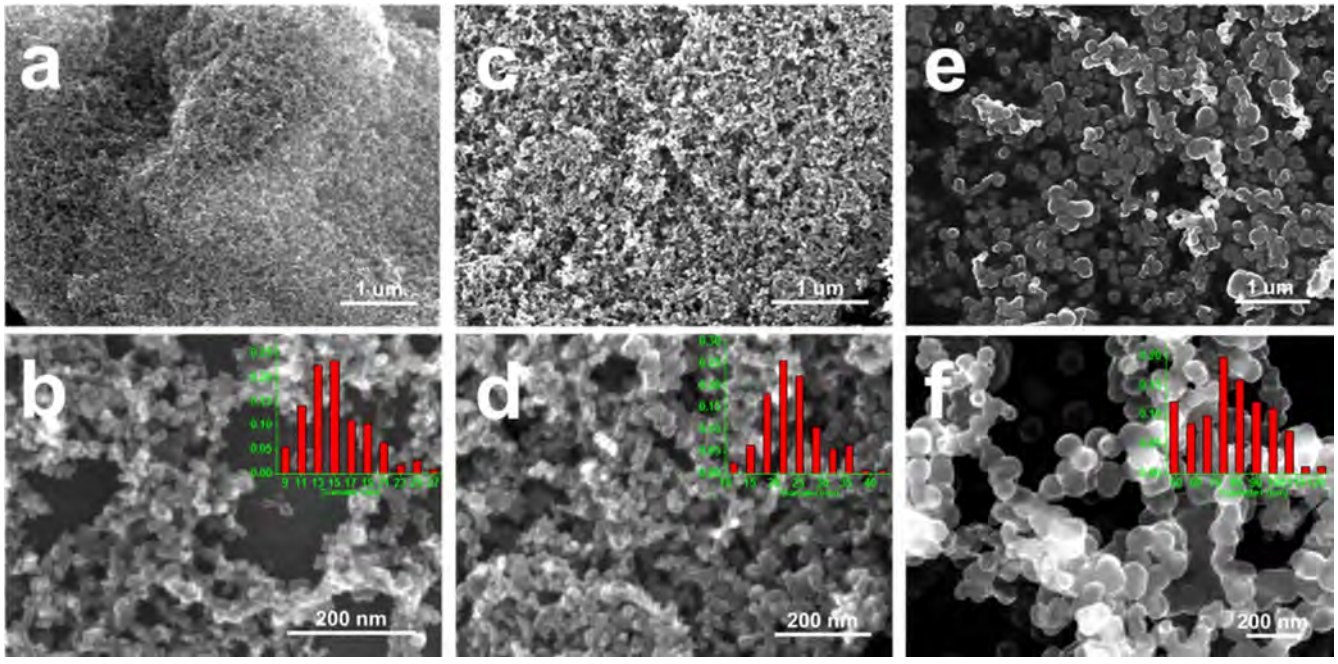

Fig. 3. SEM images of (a, b) N0-GDY, (c, d) N1-GDY and (e, f) N3-GDY at low and high magnification; the column figures in b), d), and f) are of the particle size distribution in the as-prepared GDYs.

to the G and D bands, corresponding to the E_{2g} stretching vibration mode and the breathing vibration of sp^2 carbon domains in aromatic rings. The intensity ratio of the D and G bands, I_D/I_G, is 0.75 for N0-GDY, 0.85 for N1-GDY and 0.92 for N3-GDY, respectively, indicating that N-doping produces more structural defects. It should be noted that along with the increase of the N content, there is a slightly red shift for both of the D and G band. However, there is an obvious hypochromatic shift for the Raman peak at 2179–2217 cm^{-1}, which is attributed to the vibration of conjugated diyne links (−C≡C−C≡C−), indicating the successful coupling reaction between acetylenic ends in present of air at 120 °C [1,27]. The neutron pair distribution function (PDF) can give the evidence of finding an atom at a given radius from another atom [28], and can be used to characterize partially ordered or disordered materials [29]. Further structural confirmations of the GDYs are obtained using the PDF analysis. The plots from three GDYs have similar features at the corresponding position, indicating the samples have semblable structure. We calculated the G(r) plots of the graphdiyne (two layers), graphene (two layers) and graphite based on the simulated structures from literatures [30,31]. As shown in Fig. 2d, the experimental result is more similar to the G(r) plot of the graphdiyne, especially the peak at d = 4.68 Å. This peak is recognized as the distance between the two acetylene carbon C2 and C3 which can't be found in the graphite or graphene structures. Another more prominent character is that the intensity of the first peak is stronger than the second one, which is similar with the graphdiyne model, but different from graphene and graphite. As shown in Fig. 1, the first peak is contributed by the C–C bond. The second peak is at √3 times of the C–C bond, which corresponds to the distance to the next neighbored carbon, like C1 to C1m. Apparently, more C1-C1m pairs can be observed in the graphite and graphene models. The third peak is at two times of the C–C bond, which can be attributed to the distances between the carbon atoms C1 and C1p. The presence of the peaks at 1.42 Å, 2.45 Å and 2.84 Å are the strong feature of the aromatic ring. Thus, the above achievements confirm that these precursors can be ultrafast polymerized for the formation of N-doped GDY.

According to the explosion phenomenon during the samples synthesis, the reactivity of these precursors exhibits differences, in which the explosion for N0-GDY, and N1-GDY are more violent than N3-GDY. Then, the morphologies of the as-prepared GDYs are investigated using scanning electron microscopy (SEM) for revealing the influence of the number of acetylenic group and the N-doping content (Fig. 3). Interestingly, the as-prepared samples are all featured as catenarian nanostructures, intertwining together with well 3D porous continuousness. Impressively, the particle size in the nanochain shows remarkable dependence on the molecular structure of the monomer. Replacing the benzene with pyridine or 1,3,5-triazine, the particle size will be increased from about 10 nm (N0-GDY) to 20 nm (N1-GDY), and to 80 nm (N3-GDY), indicating that the number of the acetylenic groups greatly influence the nanostructure via the reactivity of the precursors. More acetylenic groups mean higher reactivity, forming finer nanoparticles, which directly tunes the surface area of GDYs. According to the SEM testing, it is demonstrated that the GDYs have outstanding editability in morphology. The character of such 3D porous continuousness of GDYs may offer more active surface area and ion/electronic migration channels for many applications.

The GDYs nanochains are characterized by transmission electron microscopy (TEM) in Fig. 4. The large-scale images (Fig. 4a, d, and h) further disclose the 3D intertwined nanochains with good continuousness, consistent with the morphologies in above SEM measurement. According to the high-resolution TEM (HRTEM) images (Fig. 4b, e, and i), it is interestingly revealed that not only the morphologies are analogous to each other, but also the high-resolution features. It is demonstrated that all the nanoparticles for GDYs nanochains are composed of well-defined lamellas with onionlike features, indicating the highly graphitic structure of GDYs. Such onionlike all-carbon GDYs here have the mildest preparation condition than those in the literatures [32,33]. The onionlike GDY particles are connected one by one via the joint outer layers for realizing an effective 3D continuousness for

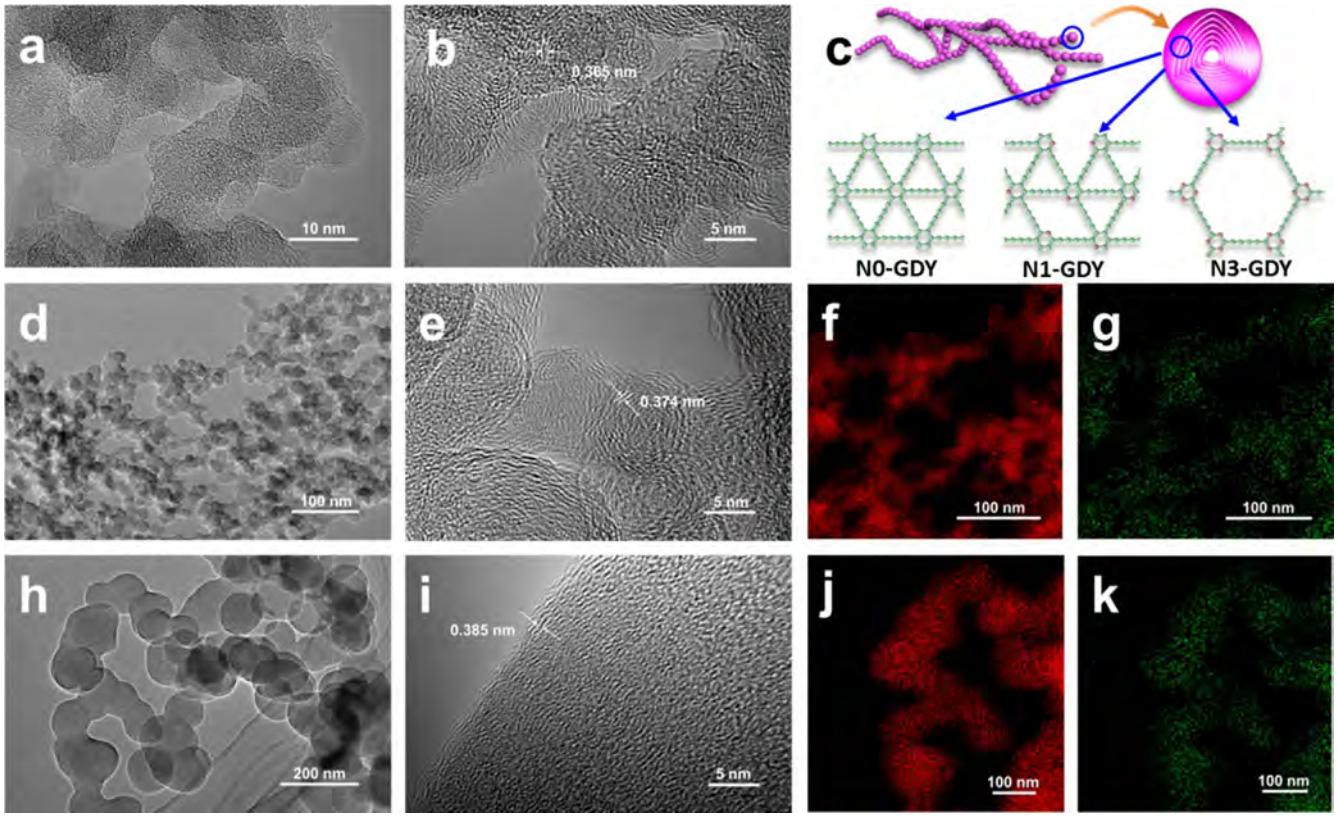

Fig. 4. TEM and HRTEM images of (a, b) GDY, (d, e) N1-GDY and (h, i) N3-GDY. EDX elemental mapping of C and N for the N1-GDY (f, g) and N3-GDY (j, k).

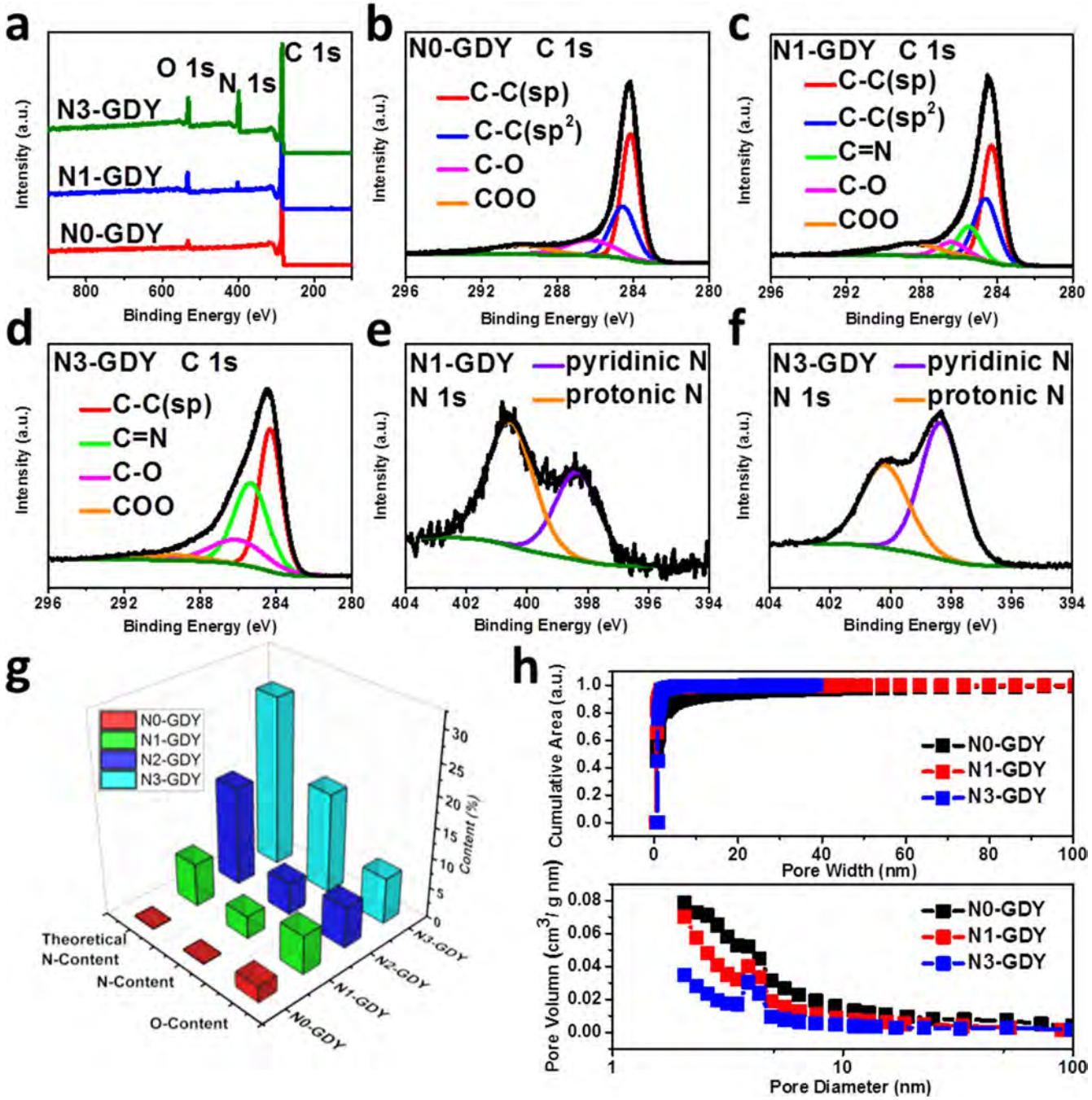

Fig. 5. (a) XPS spectra (survey) of N0-GDY, N1-GDY and N3-GDY. (b), (c) and (d) are XPS C 1s spectra of GDY, N1-GDY and N3-GDY, respectively; (e) and (f) are the XPS N 1 s spectrum of N1-GDY and N3-GDY, respectively; g) the N and O content in the as-prepared GDYs; h) pore volume and cumulative area (a. u.) of N-doped GDYs.

constructing electron transfer channels. The graphitic structure and 3D continuousness are two advantages for achieving fast response in electrochemical processes. The curved streaks with distance of 0.365 nm in N0-GDY, which can be assigned to the spacing between carbon layers, is slightly enlarged in that of N1-GDY (0.374 nm), and N3-GDY (0.385 nm), well accordant with the tendency in the XRD. The enlarged interlayer distance is probably attributed to the less electronic delocalization and weaken π-π stacking with the introduction of N atoms. Furthermore, corresponding elemental mapping in the selected areas revealed the homogeneous distribution of N as well as C in the skeletons of N1-GDY (Fig. 4f and g) and N3-GDY (Fig. 4j and k), representing the successful N-doping using this ultrafast explosion approach. This is also true for the sample N2-GDY (Fig. S2, Supporting information).

X-Ray photoelectron spectrometer (XPS) measurements were performed to confirm the elemental configurations in GDYs. In Fig. 5a, the N0-GDY is only composed of C and O elements, in which the carbon content is almost 97.35%, revealing the all-carbon nature of GDY. After N-doping, the N1-GDY and N3-GDY show obvious N characteristic peaks over 400 eV. Except for the characteristic peaks of C, O, and N for N0-GDY, N1-GDY, and N3-GDY, no signal arose from other elements, which demonstrates that such method is high-efficiently avoiding the extraneous contaminations, better than the metal-catalyzed sp^2-carbon preparation. In detail, the peak of C 1 s in N0-GDY can be mainly deconvoluted and assigned into three bonds, corresponding to sp and sp^2 at binding energy of 284.2 and 284.5 eV, C-O at 286.2 eV, and COO at 290.0 eV, respectively. After N-doping, the C1s peaks in N1-GDY and N3-GDY become wider than that of N0-GDY, because of the C=N

binding energy over 285.5 eV. The presence of element O might derive from the side reaction between unreacted acetylenic ends and oxygen, producing the C-O and COO binding energy. For N 1 s binding energy, it is obviously combined by two peaks over 398.3 (pyridinic N) and 400.2 eV (protonated N). The protonated N might be the production of pyridinic N with the neighbor carboxyl groups in the surface, as the exposed acetylenic groups in the surface will be oxidized in air. Therefore, this bottom-up method unambiguously controls the configurations of N element in the N-GDYs, showing significance than those in N-doped sp^2 carbon materials. The unambiguous N configuration in GDY offers the possibilities in accurately understanding the mechanism of N element for catalyzing, which is hard to realize in traditional N-doped sp^2 carbons materials, as various N configurations will be produced by high-temperature treatment [34]. In addition, the atomic percentage of N in the sample can be easily controlled from 3.67% (N1-GDY) to 16.55% (N3-GDY), and can be customized by mixing different precursors with demanded ratio. Impressively, this high-content of N element up to 16.55% is difficultly achieved in prevailing sp^2 carbons, and it is especially stable even at 600 °C (Fig. S3, Supporting information). The nitrogen absorption experiments are carried out to characterize the porous structure of GDYs (Fig. S4, Supporting information). Apparently, these curves indicate that these materials are type 1 porous materials in IUPAC classification, the indicative of microporous structure, with the BET surface area easily increased from 481 (N3-GDY) to 679 $m^2 g^{-1}$ (N1-GDY). Pore size distribution curves in Fig. 5h mean that the pores of GDYs are uniformly constructed with size below 5 nm, well coincident with the porous nature of GDYs. The cumulative area curves demonstrate that the surface area are mostly contributed by the micropores below 5 nm, which is good for electrochemical applications.

As a new all-carbon material with theoretically high surface area and 3D ion transfer channels, GDY has not yet been reported as supercapacitor electrode since its superiority in surface area has not yet been realized by the state-of-the-art method [1,35–37]. As seen from above measurements, the GDY samples obtained by this method possess outstanding 3D continuousness, porousness, and heteroatom doping, which are widely considered as preponderances for the powerful supercapacitor. Hence, the electrochemical properties of the GDY electrodes are characterized by cyclic voltammetry (CV) and galvanostatic charge/discharge measurements for exploring their high-power delivery performance using 7.0 M KOH aqueous electrolyte in a two-electrode symmetrical supercapacitor cell (Fig. 6, S5 and S6 of the Supporting information). As the N0-GDY and N1-GDY both have more near-rectangular CV curves and triangular charge/discharge curves (C/D) than that of N2-GDY and N3-GDY, it indicates that N0-GDY and N1-GDY have smaller resistance and better charge propagation behavior than N2-GDY and N3-GDY. The nearly rectangular-like shape of CVs with a unimpressive hump over 0.2 eV indicates that the capacitive contributions of GDYs are mostly attributed by the electric double-layer capacitance from the high surface area and pseudocapacitance from the N doping [38]. Calculated from the C/D curves, the N0-GDY and N1-GDY separately have specific capacitance of 250 and 247 F g^{-1} at 0.2 A g^{-1}, far better than N2-GDY (192 F g^{-1}) and N3-GDY (188 F g^{-1}), consistent with the specific surface area and porousness. Such a capacitance is higher than that of many sp^2 carbons obtained via the extreme experiments [39–50]. All GDYs show a fast capacitance reduction once the current density increased from 0.2 to 2 A g^{-1} and a relative stable capacitance was achieved at high current up to 40 A g^{-1}, N0-GDY, N1-GDY, N2-GDY and N3-GDY still retain 47%, 47.6%, 43.15% and 41.5% of their initial capacitance at 0.2 A g^{-1}, respectively. This phenomenon is induced by their microporous properties, as the micropore size will influence the ion accessibility and response [51,52]. The long-term stability of these electrodes are characterized by the C/D at a current rate of 5 A g^{-1}. After 3000 cycles, all supercapacitor devices show robust retention rate higher than 95.6%, indicating the GDYs have outstanding electrochemical stability as other prevailing all-carbon materials.

Fig. 7a shows the Nyquist plot of the supercapacitor obtained in the frequency range from 100 kHz to 0.1 Hz. The near-vertical feature of

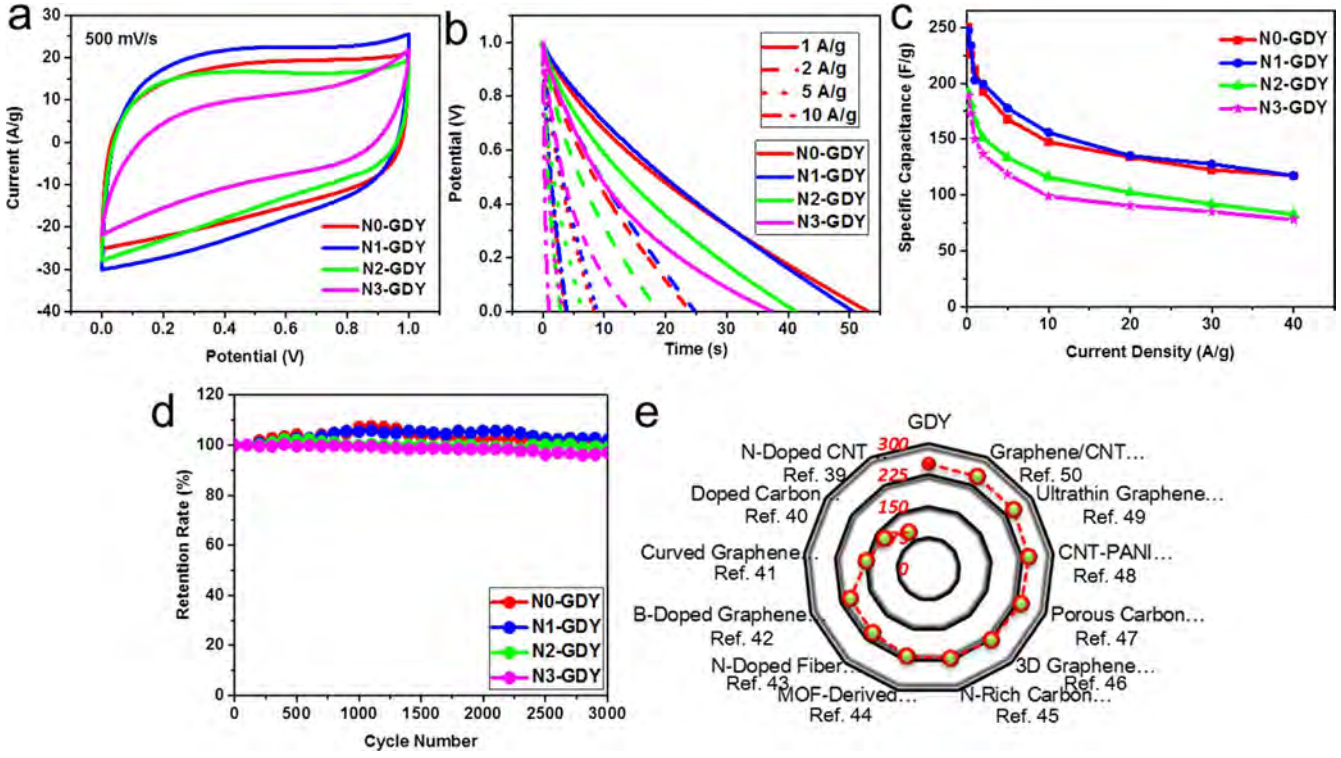

Fig. 6. Supercapacitor performance based on N0-GDY, N1-GDY, N2-GDY and N3-GDY in 7.0 M KOH aqueous electrolyte: a) Cycle voltammetry curves at a scanning rate of 500 mV s^{-1}; b) Representative Galvanostatic charge/discharge profiles under different current density; c) Specific capacitance under different current density; d) Long-term retention at a charge/discharge current density of 5 A g^{-1}; e) performance comparisons with supercapacitor electrodes in literatures by extreme conditions.

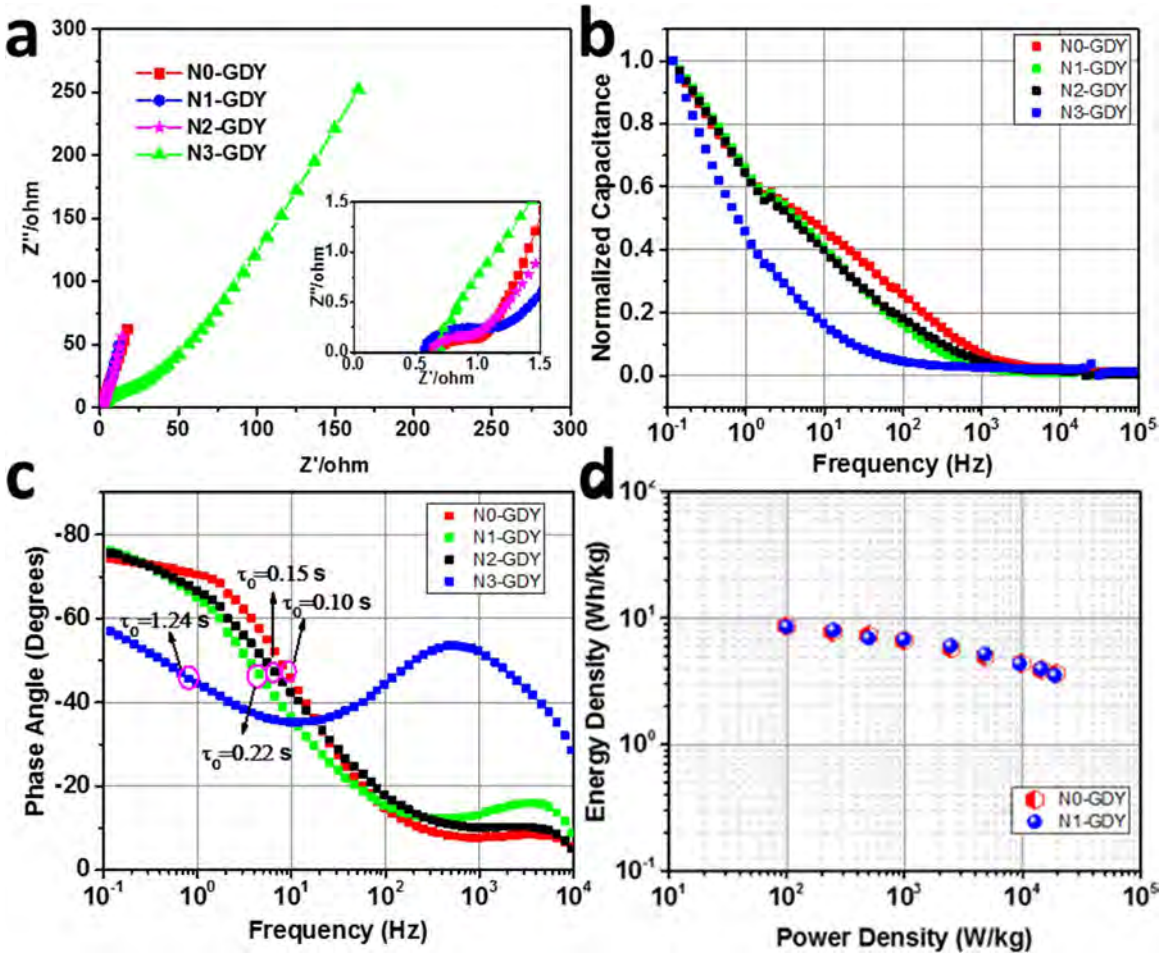

Fig. 7. a) Nyquist plot; b) Normalized capacitance as a function of frequency, and c) Bode plots of phase angle versus frequency; and d) Ragone plot showing energy density and power density.

N0-GDY and N1-GDY lines over the low frequency area, demonstrating their high capacitive performance. In the high frequency area, the plots of GDYs all intersect with the real axis at a relative low value, (0.65 Ω for N0-GDY, 0.57 Ω for N1-GDY, 0.62 Ω for N2-GDY and 0.69 Ω for N3-GDY), indicating low contact resistance with the current collectors. By extrapolating the straight line to intersect the real axis, it can be found that the N0-GDY, and N1-GDY both have a comparably low equivalent series resistance of about 1.05 Ω, explaining their similar electrochemical behavior under high current density. On the contrary, N3-GDY has the highest resistance of 25 Ω, corresponding to its relatively low performance. Fig. 7b depicts the frequency response of capacitance of GDYs, indicating that the N-doping approach dramatically influence the capacitive behavior. As shown, the characteristic frequency of GDYs at which their capacitance drops to 50% of the maximum capacitance is reduced by the addition of pyridinic N, especially for the N3-GDY samples containing 16.55% N element. Such result infers that the pyridinic N-doping strategy retard the GDYs response to fast charge/discharge behavior, which might be attributed to the depressed electronic delocalization via N-doping; and the N3-GDY has the most sluggish response because of its deeply confined electronic delocalization over the triazine structure, as aforementioned. The Bode plots of the phase angle versus frequency further disclose the N-element impact on the corresponding time constant τ_0, which shows similar tendency as above. The N0-GDY shows a comparable time constant with the reported graphene cell [53], and is pronouncedly increased by the addition of N-element in N1-GDY, N2-GDY and N3-GDY. The impedance curves of GDYs are fitted using the equivalent circuit of the Fig. S7. According to the slope of the σ_w in Fig. S8, we can find that the diffusion coefficient in the GDY, N1-GDY, and N2-GDY are obviously higher than that in N3-GDY. However, the Diffusion coefficient in N1-GDY and N2-GDY are better than GDY, indicating that the N-introduction may help improving the ion diffusion. Such results are well supported by the performance in supercapacitor. Ragone plot in Fig. 7d exhibits the energy density variation versus the power performance. As shown, the N0-GDY and N1-GDY exhibit similarly high performances, and can store the highest energy density of 8.66 (N0-GDY), and 8.55 Wh kg^{-1} (N1-GDY) and deliver the highest power density of 19.3 (N0-GDY), and 18.7 (N1-GDY) kW kg^{-1}, better than many reported performances of sp^2 carbon materials in two-electrode devices [42,54–56]. The significant improvement of the electrochemical and supercapacitor performance of GDY and N1-GDY mainly originated from the high surface area and high porosity. The morphology and impedance after cycling are obtained and shown in Fig. S9 and S10 of the Supporting information. The obtained information from the CD, impedance analysis and morphologies indicates that the supercapacitors based on the GDYs are considerably stable during the cycling tests. Considering all of the electrochemical properties, GDY and N-GDYs prepared using this mild reaction are the promising supercapacitor electrode materials.

The N-doped sp^2 carbon materials are well studied as metal-free catalyst of oxygen reduction reaction (ORR) in fuel cell for substituting the noble metal. N-doping strategy substantially improves the catalyzing reaction by facilitating the charge transfer process [57–59]. However, it still leaves controversies on understanding the catalyzing mechanism of the N-doped carbon materials, as the high-temperature doping process induces the uncertainty in controlling the N

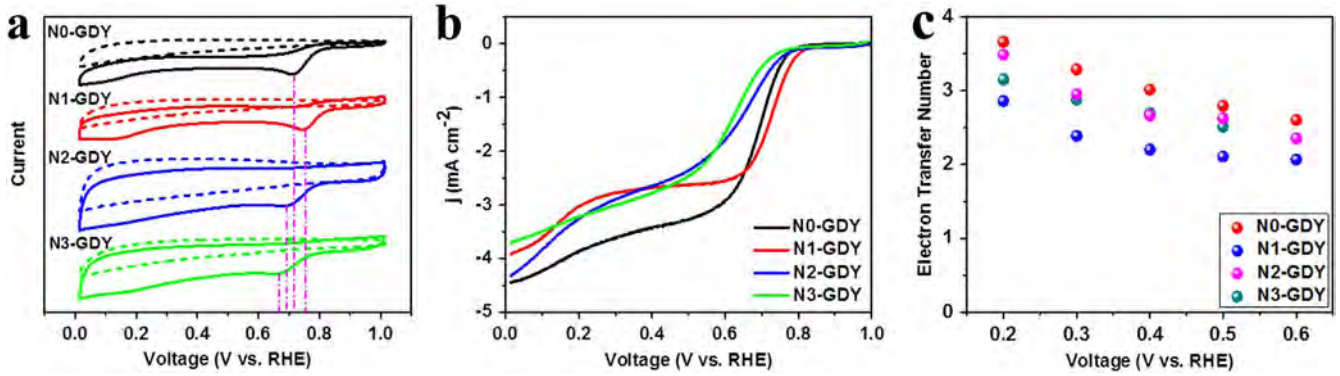

Fig. 8. a) Cyclic voltammetry (CV) of N0-GDY, N1-GDY, N2-GDY, N3-GDY, in N_2 and O_2 -saturated 0.1 M aqueous KOH solution at a scan rate of 10 mV s^{-1}, respectively; b) linear sweep voltammetry (LSV) curves in O_2-saturated 0.1 M KOH solution at a scan rate of 10 mV s^{-1}, and rotation rate is 1600 rpm; c) electron transfer number from per O_2 molecule on GDYs electrodes.

configurations in these carbon materials, and also the trace metal impurities inevitably cause dramatical interference on its performance [21]. The bottom-up way for constructing N-doped GDY cleverly avoids the above two disadvantages, undoubtedly creating N-doped GDY with well-defined N configuration without any metal impurities. Therefore, this N-doping method offers a great opportunity for well understanding the N-element roles on the GDY catalyzing performance. As shown in Fig. 8 and S11 of the Supporting information, the N-dopant remarkably impacts the onset potential of ORR; the pyridinic N push the onset potential to 0.87 V vs. RHE, 0.05 V higher than the N0-GDY (0.82 V); however, the heavy doping by triazine-like N cluster slack the ORR with the onset potential of 0.8 V, possibly ascribed to its decreased conductivity. However, the catalyzing activity is already much comparable to the graphene-based ORR catalyst [60–62], confirming that the N-doped GDY might be a new promising platform for consummating the ORR catalyst. According to the Koutecky-Levich (K-L) plot at diverse working potential, the electron transfer number from per O_2 molecule is calculated (Fig. 8d). Different with the literature [63,64], the bare N0-GDY has the best electrocatalytic efficiency than the N-doped GDYs, and can reach a four-electron-dominated ORR pathway; the introduction of N-element evidently impairs the electron transfer number. For the pyridinic N dopant, the N1-GDY mainly delivers a two-electron-transfer ORR process, probably because of the single N active center in each unit. The triazine-like N cluster partly relieves this phenomenon as there are three N active atoms in each unit, therefore, the electron transfer number is higher than that of N1-GDY over the whole working potential. Interestingly, the N2-GDY well inherits the advantages of N1-GDY and N3-GDY and its onset potential lies between those of N1-GDY and N3-GDY. Also, the synergetic effect between pyridinic N and triazine-like N cluster obviously helps to increase the electron transfer number per O_2 in N2-GDY. Via the well-defined N-doping strategy, it demonstrates that the pyridinic N dopant in GDY may be more of a hindrance than a help for ORR catalyst, and this phenomenon will probably give some useful reference on understanding the N-doped sp^2 carbons for catalyzing ORR. But, the N-dopant efficiently changes the band gap of GDY, making GDY useful all-carbon substrates for producing many high-performance composites for catalyst. From previous reported GDY-related material literature [11,65,66], it can be found that the GDYs prepared by our method feature as outstanding morphology for catalyst, because it has the best dispersibility than the reports (several micrometer). This is one of the important factor for the practical application. Also, it can be found that our catalysts can achieve a sharp increase in the current density at about −0.65 V vs. RHE, better than the abovementioned reports, indicating its possibly better power performance in the full cell.

4. Conclusion

In summary, N-doped GDY nanostructures with well-defined pyridinic N and triazine-like N cluster dopants are prepared here. We efficiently and economically control the N-content, micropores and surface area of the GDYs, demonstrating that GDY is an editable carbon material. The as-prepared GDYs have high surface area and 3D continuousness, and are assembled into two-electrode supercapacitors with specific capacitance high up to 250 F g^{-1}, delivering a high energy density (8.66 Wh kg^{-1}) and power density (19.3 kW kg^{-1}). The accurate control of the N-configuration in GDYs electrodes may provide us an opportunity to understand the N-element role in catalyzing the ORR in fuel cell. Importantly, this N-doping method may widely extend the GDY materials, and compositing with them will help exploiting their deep applications in the ever-growing new energy fields, such as fuel cells, batteries, and solar cells.

Acknowledgement

This work was supported by the National Key Research and Development Project of China (2016YFA0200104), and the Key Program of the Chinese Academy of Sciences (QYZDY-SSW-SLH015). A portion of this research used resources at the Spallation Neutron Source, a DOE Office of Science User Facility operated by the Oak Ridge National Laboratory.

Notes

The authors declare no competing financial interest.

Appendix A. Supplementary material

Supplementary data associated with this article can be found in the online version at http://dx.doi.org/10.1016/j.nanoen.2017.11.072.

References

[1] G. Li, Y. Li, H. Liu, Y. Guo, Y. Li, D. Zhu, Architecture of graphdiyne nanoscale films, Chem. Commun. 46 (2010) 3256–3258.
[2] Y. Li, L. Xu, H. Liu, Y. Li, Graphdiyne and graphyne: from theoretical predictions to practical construction, Chem. Soc. Rev. 43 (2014) 2572–2586.
[3] C. Huang, S. Zhang, H. Liu, Y. Li, G. Cui, Y. Li, Graphdiyne for high capacity and long-life lithium storage, Nano Energy 11 (2015) 481–489.
[4] Y. Xue, Y. Guo, Y. Yi, Y. Li, H. Liu, D. Li, W. Yang, Y. Li, Self-catalyzed growth of Cu@graphdiyne core–shell nanowires array for high efficient hydrogen evolution cathode, Nano Energy 30 (2016) 858–866.
[5] C. Kuang, G. Tang, T. Jiu, H. Yang, H. Liu, B. Li, W. Luo, X. Li, W. Zhang, F. Lu, J. Fang, Y. Li, Highly efficient electron transport obtained by doping PCBM with graphdiyne in planar-heterojunction perovskite solar cells, Nano Lett. 15 (2015) 2756–2762.
[6] G. Li, Y. Li, X. Qian, H. Liu, H. Lin, N. Chen, Y. Li, Construction of tubular molecule

aggregations of graphdiyne for highly efficient field emission, J. Phys. Chem. C 115 (2011) 2611–2615.
[7] R. Matsuoka, R. Sakamoto, K. Hoshiko, S. Sasaki, H. Masunaga, K. Nagashio, H. Nishihara, Crystalline graphdiyne nanosheets produced at a gas/liquid or liquid/liquid interface, J. Am. Chem. Soc. 139 (2017) 3145–3152.
[8] J. Zhou, X. Gao, R. Liu, Z. Xie, J. Yang, S. Zhang, G. Zhang, H. Liu, Y. Li, J. Zhang, Z. Liu, Synthesis of graphdiyne nanowalls using acetylenic coupling reaction, J. Am. Chem. Soc. 137 (2015) 7596–7599.
[9] H. Ren, H. Shao, L. Zhang, D. Guo, Q. Jin, R. Yu, L. Wang, Y. Li, Y. Wang, H. Zhao, D. Wang, A new graphdiyne nanosheet/Pt nanoparticle-based counter electrode material with enhanced catalytic activity for dye-sensitized solar cells, Adv. Energy Mater. 5 (2015) 1500296.
[10] H. Qi, P. Yu, Y. Wang, G. Han, H. Liu, Y. Yi, Y. Li, L. Mao, Graphdiyne oxides as excellent substrate for electroless deposition of Pd clusters with high catalytic activity, J. Am. Chem. Soc. 137 (2015) 5260–5263.
[11] R. Liu, H. Liu, Y. Li, Y. Yi, X. Shang, S. Zhang, X. Yu, S. Zhang, H. Cao, G. Zhang, Nitrogen-doped graphdiyne as a metal-free catalyst for high-performance oxygen reduction reactions, Nanoscale 6 (2014) 11336–11343.
[12] F.K. Kessler, Y. Zheng, D. Schwarz, C. Merschjann, W. Schnick, X. Wang, M.J. Bojdys, Functional carbon nitride materials-design strategies for electrochemical devices, Nat. Rev. Mater. 2 (2017) 17030.
[13] M.J. Bojdys, 2D or not 2D-layered functional (C, N) materials "Beyond silicon and graphene", Macromol. Chem. Phys. 217 (2016) 232–241.
[14] W. Wei, H. Liang, K. Parvez, X. Zhuang, X. Feng, K. Mullen, Nitrogen-doped carbon nanosheets with size-defined mesopores as highly efficient metal-free catalyst for the oxygen reduction reaction, Angew. Chem. Int. Ed. 53 (2014) 1570–1574.
[15] Y. Zhao, L. Yang, S. Chen, X. Wang, Y. Ma, Q. Wu, Y. Jiang, W. Qian, Z. Hu, Can boron and nitrogen co-doping improve oxygen reduction reaction activity of carbon nanotubes? J. Am. Chem. Soc. 135 (2013) 1201–1204.
[16] J. Tang, Y. Yamauchi, Carbon materials: mof morphologies in control, Nat. Chem. 8 (2016) 638–639.
[17] R.R. Salunkhe, C. Young, J. Tang, T. Takei, Y. Ide, N. Kobayashi, Y. Yamauchi, A high-performance supercapacitor cell based on ZIF-8-derived nanoporous carbon using an organic electrolyte, Chem. Commun. 52 (2016) 4764–4767.
[18] R.R. Salunkhe, Y.V. Kaneti, J. Kim, J.H. Kim, Y. Yamauchi, Nanoarchitectures for metal-organic framework-derived nanoporous carbons toward supercapacitor applications, Acc. Chem. Res. 49 (2016) 2796–2806.
[19] L. Wang, A. Ambrosi, M. Pumera, "Metal-free" catalytic oxygen reduction reaction on heteroatom-doped graphene is caused by trace metal impurities, Angew. Chem. Int. Ed. 52 (2013) 13818–13821.
[20] Z. Zuo, W. Li, A. Manthiram, N-heterocycles tethered graphene as efficient metal-free catalysts for an oxygen reduction reaction in fuel cells, J. Mater. Chem. A 1 (2013) 10166–10172.
[21] C. Tang, Q. Zhang, Nanocarbon for oxygen reduction electrocatalysis: dopants, edges, and defects, Adv. Mater. (2017), http://dx.doi.org/10.1002/adma.201604103.
[22] J. Neuefeind, M. Feygenson, J. Carruth, R. Hoffmann, K.K. Chipley, The nanoscale ordered materials diffractometer NOMAD at the spallation neutron source SNS, Nucl. Instrum. Methods Phys. Res. Sect. B: Beam Interact. Mater. At. 287 (2012) 68–75.
[23] C.L. Farrow, P. Juhas, J.W. Liu, D. Bryndin, E.S. Božin, J. Bloch, P. Th, S.J.L. Billinge, PDFfit2 and PDFgui: computer programs for studying nanostructure in crystals, J. Phys.: Condens. Matter 19 (2007) 335219.
[24] P. Siemsen, R. Livingston, F. Diederich, Acetylenic coupling: a powerful tool in molecular construction, Angew. Chem. Int. Ed. 39 (2000) 2632–2657.
[25] R. Liu, X. Gao, J. Zhou, H. Xu, Z. Li, S. Zhang, Z. Xie, J. Zhang, Z. Liu, Adv. Mater. 29 (2017), http://dx.doi.org/10.1002/adma.201604665.
[26] R. Schmidt, R. Thorwirth, T. Szuppa, A. Stolle, B. Ondruschka, H. Hopf, Fast, ligand- and solvent-free synthesis of 1,4-substituted buta-1,3-diynes by Cu-catalyzed homocoupling of terminal alkynes in a ball mill, Chem. Eur. J. 17 (2011) 8129–8138.
[27] X. Gao, J. Li, R. Du, J. Zhou, M.Y. Huang, R. Liu, J. Li, Z. Xie, L.Z. Wu, Z. Liu, J. Zhang, Direct synthesis of graphdiyne nanowalls on arbitrary substrates and iIts application for photoelectrochemical water splitting cell, Adv. Mater. 29 (2017), http://dx.doi.org/10.1002/adma.201605308.
[28] S.J. Billinge, M.G. Kanatzidis, Beyond crystallography: the study of disorder, nanocrystallinity and crystallographically challenged materials with pair distribution functions, Chem. Commun. (2016) 749–760.
[29] H. Zheng, K. Li, G.D. Cody, C.A. Tulk, X. Dong, G. Gao, J.J. Molaison, Z. Liu, M. Feygenson, W. Yang, I.N. Ivanov, L. Basile, J.C. Idrobo, M. Guthrie, H.K. Mao, Polymerization of acetonitrile via a hydrogen transfer reaction from CH3 to CN under extreme conditions, Angew. Chem. Int. Ed. 55 (2016) 12040–12044.
[30] N. Narita, S. Nagai, S. Suzuki, K. Nakao, Optimized geometries and electronic structures of graphyne and its family, Phys. Rev. B 58 (1998) 11009–11014.
[31] Q. Zheng, G. Luo, Q. Liu, R. Quhe, J. Zheng, K. Tang, Z. Gao, S. Nagase, J. Lu, Structural and electronic properties of bilayer and trilayer graphdiyne, Nanoscale 4 (2012) 3990–3996.
[32] Y.V. Butenko, S. Krishnamurthy, A.K. Chakraborty, V.L. Kuznetsov, V.R. Dhanak, M.R.C. Hunt, L. Šiller, Photoemission study of onionlike carbons produced by annealing nanodiamonds, Phys. Rev. B 71 (2005) 075420.
[33] T. Cabioc'h, M. Jaouen, M.F. Denanot, P. Bechet, Influence of the implantation parameters on the microstructure of carbon onions produced by carbon ion implantation, Appl. Phys. Lett. 73 (1998) 3096–3098.
[34] H. Wang, T. Maiyalagan, X. Wang, Review on recent progress in nitrogen-doped graphene: synthesis, characterization, and its potential applications, ACS Catal. 2 (2012) 781–794.
[35] S. Zhang, H. Liu, C. Huang, G. Cui, Y. Li, Bulk graphdiyne powder applied for highly efficient lithium storage, Chem. Commun. 51 (2015) 1834–1837.
[36] K. Krishnamoorthy, S. Thangavel, J.C. Veetil, N. Raju, G. Venuagopal, S.J. Kim, Graphdiyne nanostructures as a new electrode material for electrochemical supercapacitors, Int. J. Hydrog. Energy 41 (2016) 1672–1678.
[37] H. Du, H. Yang, C. Huang, J. He, H. Liu, Y. Li, Graphdiyne applied for lithium-ion capacitors displaying high power and energy densities, Nano Energy 22 (2016) 615–622.
[38] Y. Wang, Y. Song, Y. Xia, Electrochemical capacitors: mechanism, materials, systems, characterization and applications, Chem. Soc. Rev. 45 (2016) 5925–5950.
[39] F. Béguin, K. Szostak, G. Lota, E. Frackowiak, A self-supporting electrode for supercapacitors prepared by one-step pyrolysis of carbon nanotube/polyacrylonitrile blends, Adv. Mater. 17 (2005) 2380–2384.
[40] M.H. Naveen, K. Shim, M.S.A. Hossain, J.H. Kim, Y.-B. Shim, Template free preparation of heteroatoms doped carbon spheres with trace Fe for efficient oxygen reduction reaction and supercapacitor, Adv. Energy Mater. 7 (2017) 1602002.
[41] J. Luo, H.D. Jang, J. Huang, Effect of sheet morphology on the scalability of graphene-based ultracapacitors, ACS Nano 7 (2013) 1464–1471.
[42] J. Han, L.L. Zhang, S. Lee, J. Oh, K.S. Lee, J.R. Potts, J.Y. Ji, X. Zhao, R.S. Ruoff, S. Park, Generation of B-doped graphene nanoplatelets using a solution process and their supercapacitor applications, ACS Nano 7 (2013) 19–26.
[43] L.-F. Chen, X.-D. Zhang, H.-W. Liang, M. Kong, Q.-F. Guan, P. Chen, Z.-Y. Wu, S.-H. Yu, Synthesis of nitrogen-doped porous carbon nanofibers as an efficient electrode material for supercapacitors, ACS Nano 6 (2012) 7092–7102.
[44] W. Chaikittisilp, M. Hu, H. Wang, H.S. Huang, T. Fujita, K.C. Wu, L.C. Chen, Y. Yamauchi, K. Ariga, Nanoporous carbons through direct carbonization of a zeolitic imidazolate framework for supercapacitor electrodes, Chem. Commun. 48 (2012) 7259–7261.
[45] L. Hao, B. Luo, X.L. Li, M.H. Jin, Y. Fang, Z.H. Tang, Y.Y. Jia, M.H. Liang, A. Thomas, J.H. Yang, L.J. Zhi, Terephthalonitrile-derived nitrogen-rich networks for high performance supercapacitors, Energy Environ. Sci. 5 (2012) 9747–9751.
[46] Z.-S. Wu, Y. Sun, Y.-Z. Tan, S. Yang, X. Feng, K. Müllen, Three-dimensional graphene-based macro- and mesoporous frameworks for high-performance electrochemical capacitive energy storage, J. Am. Chem. Soc. 134 (2012) 19532–19535.
[47] L. Qie, W. Chen, H. Xu, X. Xiong, Y. Jiang, F. Zou, X. Hu, Y. Xin, Z. Zhang, Y. Huang, Synthesis of functionalized 3D hierarchical porous carbon for high-performance supercapacitors, Energy Environ. Sci. 6 (2013) 2497.
[48] J. Benson, I. Kovalenko, S. Boukhalfa, D. Lashmore, M. Sanghadasa, G. Yushin, Multifunctional CNT-polymer composites for ultra-tough structural supercapacitors and desalination devices, Adv. Mater. 25 (2013) 6625–6632.
[49] J.J. Yoo, K. Balakrishnan, J. Huang, V. Meunier, B.G. Sumpter, A. Srivastava, M. Conway, A.L. Mohana Reddy, J. Yu, R. Vajtai, P.M. Ajayan, Ultrathin planar graphene supercapacitors, Nano Lett. 11 (2011) 1423–1427.
[50] Y. Yang, Q. Huang, L. Niu, D. Wang, C. Yan, Y. She, Z. Zheng, Waterproof, ultrahigh areal-capacitance, wearable supercapacitor fabrics, Adv. Mater. 29 (2017) 1606679.
[51] L. Hao, X. Li, L. Zhi, Carbonaceous electrode materials for supercapacitors, Adv. Mater. 25 (2013) 3899–3904.
[52] C. Largeot, C. Portet, J. Chmiola, P.-L. Taberna, Y. Gogotsi, P. Simon, Relation between the ion size and pore size for an electric double-layer capacitor, J. Am. Chem. Soc. 130 (2008) 2730–2731.
[53] X. Yang, C. Cheng, Y. Wang, L. Qiu, D. Li, Liquid-mediated dense integration of graphene materials for compact capacitive energy storage, Science 341 (2013) 534–537.
[54] Z. Lei, N. Christov, X.S. Zhao, Intercalation of mesoporous carbon spheres between reduced graphene oxide sheets for preparing high-rate supercapacitor electrodes, Energy Environ. Sci. 4 (2011) 1866–1873.
[55] L.-F. Chen, Z.-H. Huang, H.-W. Liang, W.-T. Yao, Z.-Y. Yu, S.-H. Yu, Flexible all-solid-state high-power supercapacitor fabricated with nitrogen-doped carbon nanofiber electrode material derived from bacterial cellulose, Energy Environ. Sci. 6 (2013) 3331.
[56] Z.S. Wu, A. Winter, L. Chen, Y. Sun, A. Turchanin, X.L. Feng, K. Mullen, Three-dimensional nitrogen and boron co-doped graphene for high-performance all-solid-state supercapacitors, Adv. Mater. 24 (2012) 5130–5135.
[57] S. Wang, L. Zhang, Z. Xia, A. Roy, D.W. Chang, J.-B. Baek, L. Dai, BCN graphene as eEfficient metal-free electrocatalyst for the oxygen reduction reaction, Angew. Chem. Int. Ed. 51 (2012) 4209–4212.
[58] L. Yu, X. Pan, X. Cao, P. Hu, X. Bao, Oxygen reduction reaction mechanism on nitrogen-doped graphene: a density functional theory study, J. Catal. 282 (2011) 183–190.
[59] R. Liu, D. Wu, X. Feng, K. Müllen, Nitrogen-doped ordered mesoporous graphitic arrays with high electrocatalytic activity for oxygen reduction, Angew. Chem. Int. Ed. 49 (2010) 2565–2569.
[60] L. Qu, Y. Liu, J.-B. Baek, L. Dai, Nitrogen-doped graphene as efficient metal-free electrocatalyst for oxygen reduction in fuel cells, ACS Nano 4 (2010) 1321–1326.
[61] S. Wang, D. Yu, L. Dai, D.W. Chang, J.-B. Baek, Polyelectrolyte-functionalized graphene as metal-free electrocatalysts for oxygen reduction, ACS Nano 5 (2011) 6202–6209.
[62] Y. Zhao, C. Hu, Y. Hu, H. Cheng, G. Shi, L. Qu, A versatile, ultralight, nitrogen-doped graphene framework, Angew. Chem. Int. Ed. 51 (2012) 11371–11375.
[63] Z.J. Wang, R.R. Jia, J.F. Zheng, J.G. Zhao, L. Li, J.L. Song, Z.P. Zhu, Nitrogen-promoted self-Assembly of N-doped carbon nanotubes and their intrinsic catalysis for oxygen reduction in fuel cells, ACS Nano 5 (2011) 1677–1684.
[64] Z.-H. Sheng, L. Shao, J.-J. Chen, W.-J. Bao, F.-B. Wang, X.-H. Xia, Catalyst-free synthesis of nitrogen-doped graphene via thermal annealing graphite oxide with melamine and its excellent electrocatalysis, ACS Nano 5 (2011) 4350–4358.

[65] S. Zhang, Y. Cai, H. He, Y. Zhang, R. Liu, H. Cao, M. Wang, J. Liu, G. Zhang, Y. Li, H. Liu, B. Li, Heteroatom doped graphdiyne as efficient metal-free electrocatalyst for oxygen reduction reaction in alkaline medium, J. Mater. Chem. A 4 (2016) 4738–4744.

[66] Q. Lv, W. Si, Z. Yang, N. Wang, Z. Tu, Y. Yi, C. Huang, L. Jiang, M. Zhang, J. He, Y. Long, Nitrogen-doped porous graphdiyne: a highly efficient metal-free electrocatalyst for oxygen reduction reaction, ACS Appl. Mater. Interfaces 9 (2017) 29744–29752.